Available online at www.sciencedirect.com
ScienceDirect
Acta Materialia 57 (2009) 3020–3028
Acta MATERIALIA
www.elsevier.com/locate/actamat

Measurement of the local mechanical properties in polycrystalline samples using spherical nanoindentation and orientation imaging microscopy

Siddhartha Pathak [a,b], Dejan Stojakovic [a], Surya R. Kalidindi [a,*]

[a] Department of Materials Science and Engineering, Drexel University, 3141 Chesnut Street, Lebow 344, Philadelphia, PA 19104, USA
[b] EMPA – Swiss Federal Laboratories for Materials Testing and Research, Feuerwerkerstrasse 39, CH-3602 Thun, Switzerland

Received 17 December 2008; received in revised form 2 March 2009; accepted 3 March 2009
Available online 11 April 2009

Abstract

This paper describes the development of novel experimental protocols and data analysis procedures for extracting meaningful indentation stress–strain curves from spherical nanoindentation on polycrystalline samples, and correlating these measurements to the local crystal lattice orientation measured by orientation imaging microscopy at the indentation site. In particular, we demonstrate that it is possible to estimate the percentage increases in the local slip resistance in deformed samples of polycrystalline cubic metals from their fully annealed condition. These novel procedures are demonstrated on Fe–3% Si samples in the as-cast, 30% deformed and 80% deformed conditions.

Keywords: Nanoindentation; Orientation imaging microscopy (OIM); Metal and alloys – steel; Yield phenomena; Slip resistance

1. Introduction

Nanoindentation [1,2], with its high resolution load and depth sensing capabilities, is being used increasingly to characterize the local mechanical behavior at ever-decreasing scales of interest in a broad range of materials systems with heterogeneous microstructures. This technique has been traditionally used for characterizing the local hardness [3] using sharp indenters [4,5]. However, our recent work [6,7] has demonstrated the tremendous potential to transform the raw load–displacement data obtained using spherical indenters into meaningful indentation stress–strain curves. These newly developed indentation data analysis methods have successfully captured the local loading and unloading elastic moduli, the local indentation yield strengths and certain aspects of post-yield strain hardening behavior in polycrystalline aluminum and tungsten samples [6,8]. They have also been found to be very useful in identifying and explaining several of the surface preparation artifacts typically encountered in the nanoindentation measurements [9]. Because the length scales in nanoindentation are smaller than the typical crystallite (also called grain) sizes in polycrystalline samples, this technique is an ideal tool for detailed characterization of the microscale heterogeneities present in these materials and their evolution during various metal shaping/working operations.

In this paper, we report on the development and validation of the nanoindentation data analysis procedures with the specific aim of characterizing the local indentation yield strengths in individual grains of deformed polycrystalline metallic samples and relating them to increases in the local slip resistances. Our focus in this paper will be on cubic metals. It is well known that metals harden significantly with the imposition of plastic strain (especially when deformed at low homologous temperatures; also called cold-working). However, as a result of the grain-scale heterogeneity

* Corresponding author.
E-mail address: skalidin@coe.drexel.edu (S.R. Kalidindi).

1359-6454/$36.00
doi:10.1016/j.actamat.2009.03.008

in their microstructures, the individual grains do not harden equally. In spite of some reported experimental and modeling studies to understand the development of deformed microstructures in polycrystalline cubic metals [10–13], there remains a critical need for the development of novel methods to characterize the local changes in the yield strength in the individual grains of a polycrystalline metallic sample as a function of the macroscale plastic deformation imposed on the sample. Nanoindentation offers tremendous promise for addressing this critical need. However, it requires development and validation of the data analysis methods that account rigorously for the inherent dependence of the indentation yield strength on the local crystal lattice orientation. For example, it is fully expected that the indentation yield strength will vary significantly from one crystal orientation to another, even in fully annealed samples where there are no major differences in the dislocation content of the differently oriented grains. This is because the plastic deformation imposed by the indenter needs to be accommodated locally at the indentation site by slip activity on the available slip systems, whose orientation and activation are strongly dependent on the local crystal lattice orientation with respect to the indentation direction. Therefore, a rigorous methodology is needed to account for the effect of the crystal lattice orientation on the indentation yield strength so that we can reliably establish the contribution to the indentation yield strength from the dislocation content at the indentation site. If we can successfully decouple the effects of orientation from the effects of the increased dislocation density on the local measurements of indentation yield strength, it should be possible to estimate the local percentage increase in the average slip resistance at the indentation site.

One of the challenges arises from the fact that the mechanical response of individual grains is inherently anisotropic, whereas almost all nanoindentation data analysis methods are built on Hertz's theory [14], which assumes an isotropic elastic material behavior. As shown in this paper, the indentation response of Fe–3% Si steel can be adequately captured by using a modified form of Hertz's analyses for elastically anisotropic cubic materials, originally proposed by Vlassak and Nix [15,16]. It is also important to recognize that it is necessary to extract the local indentation yield strength from an analysis of the initial loading segment in the indentation experiment, because the indentation itself will alter the local microstructure and its properties once it imposes additional local plastic deformation.

It will be shown in this paper that the average increase in the local slip resistance at the indentation site in the deformed polycrystalline microstructures can be characterized by combining the capabilities of spherical nanoindentation and orientation imaging microscopy (OIM) (this basic idea was briefly introduced in a prior study from our research group [17]). OIM is based on automated indexing of back-scattered electron diffraction patterns (obtained using a scanning electron microscope) and has a spatial resolution of less than a micron.

2. Materials and methods

Polycrystalline samples of Fe–3% Si steel, which is known to exhibit substantial elastic anisotropy ($A = 2.84$) and plastic anisotropy on the scale of individual grains, were used in this study. The samples were sectioned by electric discharge machining from the chill zone of a directionally solidified electrical steel ingot. These samples were chosen because they exhibited extremely large grains (of the order of few millimeters in effective grain size). The large grains significantly reduce the chances for the existence of a grain boundary just below the surface at the indentation site, especially when the indentations are performed in the central parts of large grains. It should be noted that the OIM technique probes essentially the top surface of the samples, and is therefore unable to detect subsurface details of the microstructure. Some of the samples were given a 30% reduction in simple compression to produce a moderately deformed microstructure; other samples were subjected to 80% reduction in plane strain compression to produce a heavily deformed microstructure. Both of these deformations were applied at room temperature using an Instron (Frame 1127R) screw-driven testing machine. During these deformations, all contact surfaces between the sample and the dies were lubricated with graphite-based grease and a 0.1 mm thick Teflon sheet.

The samples (as-cast as well as deformed) were first prepared for OIM using a Buehler grinding and polishing machine. After grinding by Si-C papers, 3 and 1 μm diamond suspensions were used for polishing the samples in conjunction with several intermediate etches by Nital (5 vol.% mixture of nitric acid in ethanol). The samples were subsequently polished using 0.05 μm colloidal silica. The final step included vibratory polishing with 0.02 μm colloidal silica on a Buehler vibratory polisher for several (2–4) days. Note that a high-quality final surface finish is absolutely essential for both the OIM measurements and the subsequent indentation experiments. Whenever this detailed sample preparation protocol was not followed carefully, we often observed that the measurements were prone to large errors. This problem has been discussed in detail in our recent publication [9]. It is reiterated here that the final surface preparation step with the vibratory polisher for a few days is of utmost importance, as it produced a smooth surface, comparable to electropolishing, that appears to be free of any additional strain due to the sample preparation techniques themselves [18].

Nanoindentations were carried out using a nanoindenter (MTS XP® System equipped with the continuous stiffness measurement (CSM) attachment) with a 13.5 μm radius spherical diamond tip. The tests were carried out under load control to peak displacements of 150 nm in all samples. The nanoindentation test points were chosen at the middle of the individual grains, well away from the grain boundaries, in order to mitigate any influence of the grain boundaries on the test results.

3. Data analysis methods for spherical indentation

Transforming the measured load–displacement data in spherical nanoindentation into indentation stress–strain curves allows a more transparent and efficient way of analyzing the local material behavior. These indentation stress–strain curves allow a better identification of the different stages of material behavior under contact loading, particularly during the loading segment of the indentation process. Our recent reports illustrate how the indentation stress–strain curves can be used to capture a wealth of information about the material, including the elastic moduli measured in loading and unloading segments [6–8], the elastic limit (which can be identified as yielding in metallic samples [6,8,9] or buckling in a high aspect ratio material like carbon nanotubes [19]), different aspects of the post-elastic behavior [6,8], as well as identifying and explaining several of the surface preparation artifacts typically encountered in nanoindentation measurements [9].

Our analysis procedures are detailed in Ref. [6] and can be briefly summarized as a two-step procedure. The first step in the analysis process is an accurate estimation of the point of effective initial contact in the given data set, i.e. a clear identification of a zero-point that makes the measurements in the initial elastic loading segment consistent with the predictions of Hertz's theory [2,14,20]. As shown in Ref. [6], the zero-point can be conveniently determined using the following equation for the initial elastic segment in a frictionless, spherical indentation:

$$S = \frac{3P}{2h_e} = \frac{3(\tilde{P} - P^*)}{2(\tilde{h}_e - h^*)} \tag{1}$$

where $\tilde{P}$, $\tilde{h}_e$ and S are the measured load signal, measured displacement signal and CSM signal in the initial elastic loading segment from the machine, respectively, and P^* and h^* denote the values of the load and displacement values at the point of effective initial contact. Rearrangement of Eq. (1) reveals that a plot of $\tilde{P} - \frac{2}{3}S\tilde{h}_e$ against S will produce a linear relationship whose slope is equal to $-\frac{2}{3}h^*$, with the y-intercept equal to P^*. A linear regression analysis can then be performed to identify the point of the effective initial contact ($P^*$and h^*) very accurately.

Next, the values of indentation stress and strain can be calculated by recasting Hertz theory for frictionless, elastic, spherical indentation as

$$\sigma_{ind} = E_{eff}\varepsilon_{ind}, \qquad \sigma_{ind} = \frac{P}{\pi a^2}, \qquad \varepsilon_{ind} = \frac{4}{3\pi}\frac{h_e}{a} \approx \frac{h_e}{2.4\,a},$$
$$a = \frac{S}{2E_{eff}}, \qquad \frac{1}{E_{eff}} = \frac{1-\nu_s^2}{E_s} + \frac{1-\nu_i^2}{E_i}, \qquad \frac{1}{R_{eff}} = \frac{1}{R_i} + \frac{1}{R_s} \tag{2}$$

where σ_{ind} and ε_{ind} are the indentation stress and indentation strain, a is the radius of the contact boundary at the indentation load P, h_e is the elastic indentation depth, S ($= dP/dh_e$) is the elastic stiffness described earlier, R_{eff} and E_{eff} are the effective radius and the effective stiffness of the indenter and the specimen system, ν and E are the Poisson's ratio and the Young's modulus, and the sub-

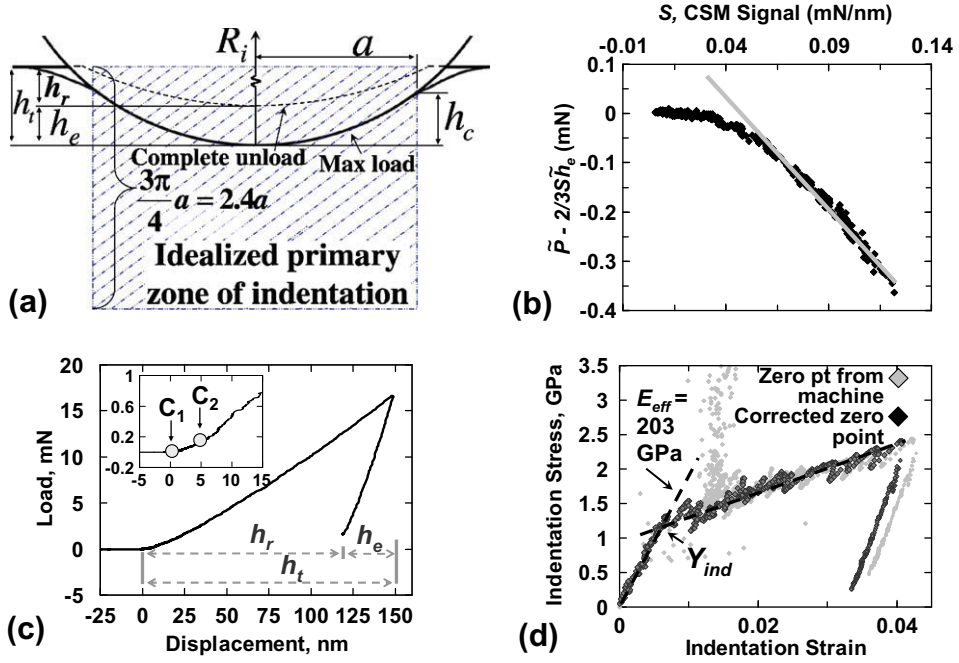

Fig. 1. (a) Schematic of a spherical indentation showing the primary zone of indentation. (b) The identification of the effective zero-point following the linear regression analysis method described in Ref. [6]. (c) The measured load–displacement curve and (d) the extracted indentation stress–strain curves for Fe–3% Si steel are shown here using two different estimates of the zero-point. The use of the zero-point established by the machine (C_1) results in an unexplainable spike in the initial elastic loading portion of the curve. When the effective zero-point (C_2) is determined using Ref. [6], much better indentation stress–strain curves are obtained. (d) also shows the back-extrapolation method used to estimate the indentation yield strength.

scripts s and i refer to the specimen and the indenter, respectively (see also Fig. 1a).

Hertz's theory (expressed here as Eqs. (1) and (2)) addressed only the elastic indentation of an isotropic sample. However, in practice, the elastic response of the sample at the typical length scale of nanoindentation is often inherently anisotropic, especially in polycrystalline metals, where the indents are much smaller than the typical grain sizes. Several researchers have employed grossly simplified treatments of anisotropy in the analyses of the nanoindentation data (e.g. the use of effective isotropic elastic properties [21] or the use of elastic modulus in the direction of indentation [22]). More recently, Vlassak and Nix [15,16,23,24] have provided a much more rigorous treatment of the theory of the elastic indentation of anisotropic samples. These authors suggest that Eq. (2) can be used for elastic indentation of cubic crystals, provided that an anisotropy parameter, β, is appropriately introduced into the definition of the effective indentation modulus. In particular, they suggest that Eq. (2) be modified as

$$\frac{1}{E_{eff}} = \frac{1}{\beta}\left(\frac{1-\nu_s^2}{E_s}\right) + \left(\frac{1-\nu_i^2}{E_i}\right) \tag{3}$$

where E_s and ν_s denote the effective values of Young's modulus and Poisson's ratio, respectively, for a randomly textured polycrystalline aggregate of crystals with the same elastic properties as the single crystal being studied [15,16]. For cubic crystals, the value of β depends strongly on the crystal lattice orientation and the degree of cubic elastic anisotropy. The elastic anisotropy of a cubic crystal is usually defined by $A = 2C_{44}/(C_{11} - C_{12})$, where C_{11}, C_{12} and C_{44} denote the cubic elastic constants used to define the crystal elastic stiffness in its own reference frame. The values of the parameter β have been analytically computed and validated for a few special (symmetric) lattice orientations. Based on the values reported by Vlassak and Nix [15,16], the values of β should be in the range of 0.9–1.1 for Fe–3% Si crystals (for which $A = 2.84$) of different orientations. In the present study, we have performed indentations on a broad range of crystal orientations in Fe–3% Si and validated the linear relationship between the indentation stress and the indentation strain (defined in Eq. (1) and modified by the introduction of β in Eq. (3)) in the elastic loading regime, as well as the values of β predicted by Vlassak and Nix [15].

The following points need to be noted when using Eqs. (1)–(3):

(i) The use of Eq. (1) is made possible due to the CSM option in the MTS Nanoindenter XP®, which provides the S signal as an independent measurement. When using an indentation machine without the CSM option, a different procedure needs to be followed, as detailed in Ref. [8].

(ii) $P^*$and h^* values, as obtained from the nanoindenter machine, are not necessarily zero. In other words, the accuracy of the zero-point established by the software using its default approach is often inadequate [25–33]. This assumes special significance in the present work since it is necessary to extract the local indentation yield strength from an analysis of the initial loading segment in the indentation experiment because the indentation itself will alter the local microstructure of the metal and its properties once it imposes additional local plastic deformation. The gravity of the problem is immediately evident when one considers the range of reported errors in the zero-point measurement in nanoindentation (anywhere from ±2 nm [33] to ±30 nm [34]) compared to the typical elastic loading depth in spherical nanoindentation (20-40 nm [6,8]). This point is further illustrated in Fig. 1b and c. The regression analysis performed on a typical dataset to identify the effective point of initial contact is shown in Fig. 1b. The points of initial contact, as identified by the default procedure in the MTS software (C_1) and by our analysis described earlier (C_2) for this dataset, are displayed in Fig. 1(c). It was noted that the load signal had to be moved by about 0.09 mN and the displacement signal by about 4.8 nm with respect to C_1 to arrive at C_2. After this small shift, the corrected load–displacement curve in the initial elastic loading segment was found to be in excellent agreement with Hertz's theory (as presented in Eqs. (1) and (2)). Note that $h_e = h_t$ and $R_{eff} = R_i$ in this relatively short initial loading segment, and it is fairly straightforward to estimate a value of E_{eff} by fitting the corrected load–displacement curve to Eq. (2).

(iii) Eq. (1) identifies an "effective" point of initial contact – the values of P^* and h^* relate to a virtual flat surface free from any sample preparation artifact, like surface roughness. More importantly, it also allows us to de-emphasize the oxide layer routinely present on the steel samples used in this study.

(iv) A further major advantage of the approach outlined in Eq. (1) is the fact that this method does not warrant any prior knowledge of the values of R_{eff} and E_{eff}. This is the main reason we are able to simply extend the procedure we used previously for elastically isotropic materials to the elastically anisotropic materials studied here.

(v) As a final note, it is pointed out that the indentation strain definition used in Eq. (2) is substantially different from the a/R_{eff} definition used in many prior studies [35–39]. This new definition of indentation strain has been validated many recent studies [6–9,19] using both numerical simulations and direct experimental measurements. Briefly, it is pointed out here that a/R_{eff}, or the more commonly used a/R_i (because of the difficulties in measuring R_{eff}), lacks any reasonable physical interpretation as a strain measure (classically defined as the ratio of change in length over the initial length of a selected line segment in a region of interest in the sample). The new definition of

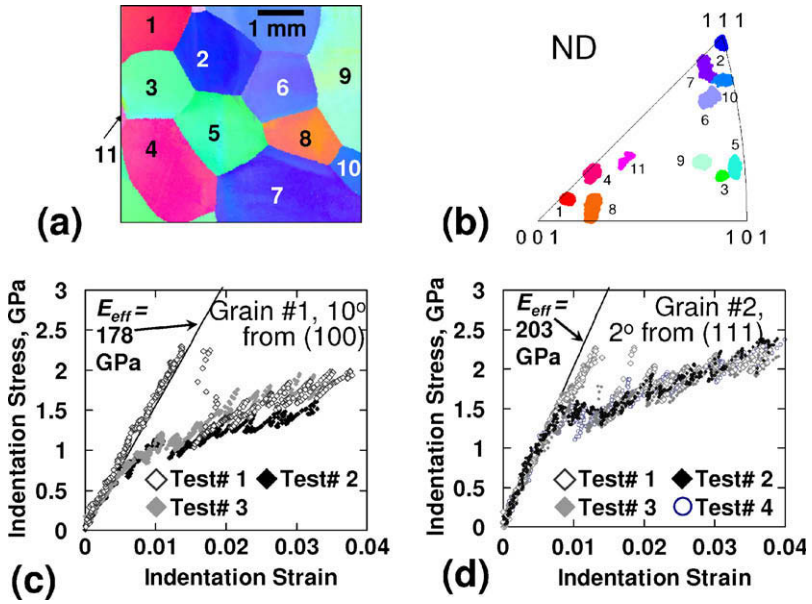

Fig. 2. (a) OIM scan and (b) inversed pole figure map obtained on a sample of annealed and polished Fe–3% Si showing a wide range of grain orientations. The measured stress–strain curves on grain #1 and grain #2, shown in (c and d), respectively, demonstrate the consistency of the nanoindentation measurements.

indentation strain presented in Eq. (1) is tantamount to idealizing the primary zone of indentation deformation, as shown in Fig. 1a. The indentation is idealized here as being equivalent (in an average sense) to compressing by h_e (same as the total indentation depth, h_t, for a purely elastic indentation) a cylindrical region of radius a and height 2.4 a. These observations have led us to propose the use of $\frac{h_t}{2.4\,a}$ as the definition of indentation strain, when generalized for elastic–plastic indentations [6–9,19].

The indentation stress–strain curve for the selected data set, computed using the procedures described above, is shown in Fig. 1d. It is seen that the data analysis procedures described here produce a much better description of the initial loading segment (i.e. no spikes in the initial loading segment). In particular, for the data set shown, the value of E_{eff} was estimated to be 203 GPa. This is in excellent agreement with the theory presented by Vlassak and Nix [15], which predicts that this value should be in the range of 170–204 GPa for Fe–3% Si ($A = 2.84$), depending on the crystal lattice orientation at the indentation site. Results for specific crystal orientations are presented and discussed in the next section. The value of the indentation yield strength, Y_{ind}, is established in this work using a back-extrapolation method, as shown in Fig. 1d.

Note that the calculation of Y_{ind} using the above back-extrapolation method is crucial in determining the onset of plastic deformation in a bulk region of the sample – a region in which the indentation zone size (see Fig. 1a) is larger than the dislocation length scales in the sample (e.g. spacing of dislocations, dislocation cell size). If this condition is not met, as happens when indenting an annealed metallic sample with a small indenter, displacement bursts, or "pop-ins", are observed. These pop-ins can be attributed to the difficulty of activation of a dislocation source in the material in the primary indentation zone. This issue has been discussed in detail in our recent report [9]. Note that the extremely high stresses at pop-in are an artifact of the interplay between the indentation zone and the average defect density of the sample, and as such are not representative of the yield strength of the bulk material. Pop-ins can be avoided by the use of indenters with large radii, where the indentation zones are substantially larger than the average dislocation spacing. The use of the 13.5 μm radius spherical indenter in this work thus helps to minimize the propensity of pop-ins in the Fe–3% Si samples studied here. In some tests that still show pop-ins (as seen in Fig. 2a and b), the back-extrapolation method helps to estimate a global Y_{ind} value, instead of the pop-in stress.

4. Results and discussion

As described earlier, an as-cast polycrystalline sample of Fe–3% Si steel with very large grains was used in this study. The OIM scan obtained on this sample is shown in Fig. 2a. The grain orientations are color-coded to reflect their positions in the inverse pole figure map provided in Fig. 2b. For example, the grains that have a (0 0 1) crystallographic plane parallel to the sample surface are colored red.[1] Because we are studying cubic crystals, this also means that the grains colored red have a [0 0 1] crystallographic direction parallel to the sample normal direction (ND; also the

[1] For interpretation of color in Fig. 2, the reader is referred to the web version of this article.

indentation direction). In a similar manner, grains with a (1 0 1) plane parallel to the surface are colored green, while the grains with a (1 1 1) plane parallel to the surface are colored blue. It is seen that the selected region of the sample has a range of grain orientations that provide a good coverage of the corners of the fundamental triangle in the inverse pole figure for cubic crystals. Because of the very large grain sizes in the sample, we can assume that the indentation measurements in any one grain are unlikely to be influenced by the neighboring grain orientations or grain boundaries.

The indentation measurements conducted in this study showed the largest difference in the indentation stress–strain curves of the near-(1 1 1)-oriented grains and the near-(0 0 1)-oriented grains, with the response of the near-(1 0 1)-oriented grains being fairly close to the response of the near-(1 1 1)-oriented grains. Fig. 2c and d shows representative indentation stress–strain curves obtained from multiple indentations in two of the grains studied. It is observed that the measurements in each grain are highly consistent with each other, except for the occurrence of pop-ins that result in an extended initial linear elastic segment. Interestingly, it is also observed that the indentation stress–strain curve after the pop-in event is very much consistent with the measurements obtained without the pop-in events. The physical origin of the pop-in events will be discussed later.

The table in Fig. 3a summarizes the measured values of the effective indentation stiffness, the anisotropic elasticity parameter, β, and the back-extrapolated indentation yield strengths, Y_{ind}, in the 11 different grain orientations studied. In computing the values of β, the values of E_s and v_s have been taken as 207.9 GPa and 0.3 following the approach described in Refs. [15,40]. The orientations of the grains studied are provided here using Bunge–Euler angles [41]. It is observed that the near-(0 0 1)-oriented grains exhibit the lowest indentation moduli and the lowest indentation yield strengths, while the near-(1 1 1)-oriented grains exhibit the highest indentation moduli and indentation yield strengths. The measured differences in the indentation moduli range from a minimum of $\beta = 0.92$ (grain #1) to a maximum of $\beta = 1.12$ (grain #2). These measurements are highly consistent with the values predicted by Vlassak and Nix [15]. These authors predicted a value of 0.9 for (0 0 1)-oriented grains, 1.10 for (1 0 1)-oriented grains and 1.1 for (1 1 1)-oriented grains based on an anisotropy factor of $A = 2.84$ for Fe–3% Si.

An important observation from the table in Fig. 3a is that the differences in the measured indentation yield strengths of different grain orientations are as high as 30%. Since there are no expected differences in the dislocation content of the differently oriented large grains in the as-cast sample studied here, all of the observed differences in the indentation yield strengths are attributable to differ-

(a)

Fe-3%Si As-cast						
	Grain No.	Orientation (φ_1, Φ, φ_2)	Misorientation	E_{eff}, GPa	β	Y_{ind}, GPa
Near (111)	2	339.8, 54.4, 46.1	2° from (111)	202.9±4.10	1.12	1.13±0.04
	7	103.7, 121.6, 49.9	9° from (111)	199.3±1.24	1.09	1.12±0.02
	10	232.5, 53.1, 324.0	10° from 111)	197.7±2.06	1.08	1.12±0.16
	6	83.2, 125.4, 30.4	14° from (111)	195.9±1.90	1.07	1.10±0.02
Near (101)	3	3.0, 41.3, 76.4	11° from (101)	194.0±2.62	1.05	1.09±0.04
	5	194.7, 79.7, 317	14° from (101)	191.1±1.49	1.04	1.07±0.01
	9	50.0, 38.1, 250.1	16° from (101)	190.5±3.05	1.03	1.06±0.02
Near (001)	1	114.2, 85, 173.5	10° from (001)	173.2±2.20	0.92	0.85±0.04
	8	170.0, 102.6, 357.9	15° from (001)	178.3±1.23	0.95	0.91±0.06
	4	163.6, 78.8, 168	18° from (001)	181.2±1.07	0.97	0.93±0.04
	11	259.9, 238.0, 145.8	26° from(001)	189.6±1.26	1.03	1.0±0.06

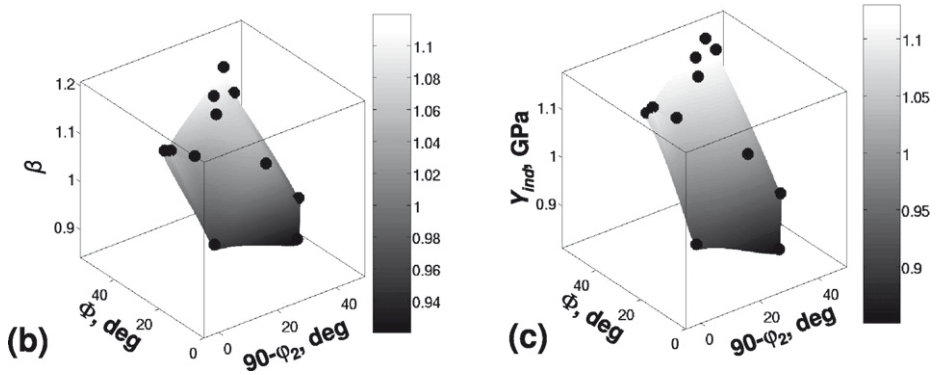

Fig. 3. The table in (a) shows the different orientations of the 11 grains studied in this work in terms of their Bunge-Euler angles and the measured values of the effective indentation modulus E_{eff}, the anisotropic elasticity parameter β, and the back-extrapolated indentation yield strengths Y_{ind} in these grains. (b) and (c) show the surface contour plots of β and Y_{ind} obtained by interpolating the values reported in (a).

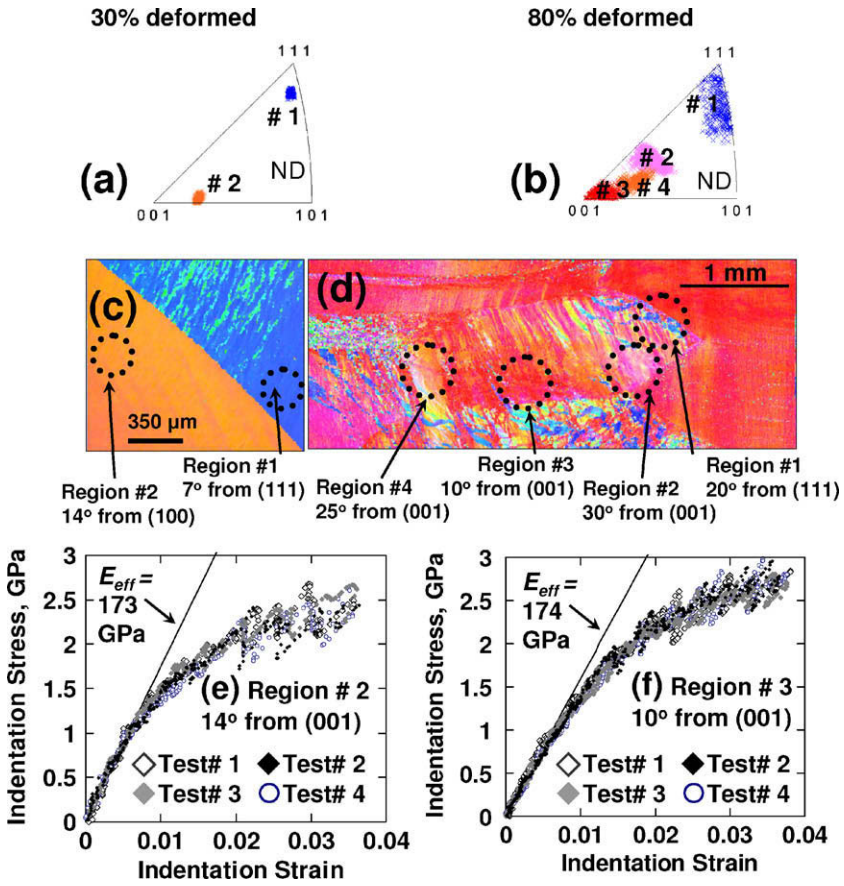

Fig. 4. (a and c) The inverse pole figure map and the OIM scan for a 30% deformed Fe–3% Si sample due to compression; (b and d) the same for a 80% deformed sample. Indentations were performed in the regions marked by the dotted circles in each of these samples. (e) The measured multiple indentation stress strain curves for region #2 in the 30% deformed sample; (f) the same for region #3 in the 80% deformed sample. Note the consistency of the indentation stress–strain curves in (e and f).

ences in the activities of the different slip systems in the different grains and their orientation with the indentation direction. It is also pointed out that the scatter in the measurements in each grain is fairly low.

The grain orientation is in general described by a set of three angles called Bunge–Euler angles [41]. These are usually denoted as (φ_1, Φ, φ_2). Since the rotation of the sample about the normal to the indentation surface (i.e. the ND direction) does not influence the measurements presented here, the indentation modulus and the indentation yield strengths measured here using a spherical indenter are functions of only two of the Bunge–Euler angles, namely (Φ, φ_2). Fig. 3b and c shows the contoured surface plots of the dependence of the β and the indentation yield strength, respectively, on the grain orientation that are obtained by interpolating the values reported in Fig. 3a. The value of these plots (especially the plot for indentation yield strength) will become clear as we discuss the data analysis methods for deformed samples.

As described earlier, a major goal of our study is to develop and validate methods for characterizing the increases in the indentation yield strengths in individual crystals of deformed polycrystalline samples from their corresponding values in the as-cast condition. When the sample is plastically deformed, grains undergo significant lattice rotations and typically break down into smaller grains. In this study, we subjected one of the as-cast samples to 30% reduction in simple compression and another as-cast sample to 80% reduction in plane strain compression. These reduction levels were selected to produce one moderately deformed sample and one heavily deformed sample. Orientation maps were obtained for both deformed microstructures using the OIM technique and are shown in Fig. 4a–d. Indentations were performed in selected regions within individual grains in each of the deformed samples. In both samples, we found several regions in the near-(0 0 1)- and near-(1 1 1)-oriented grains, but not in the near-(1 0 1)-oriented grains. Indentation stress–strain curves from representative regions in these deformed samples are shown in Fig. 4e and f. It is once again observed that the multiple measurements from the same grain produce highly consistent indentation stress–strain curves. It is also noted that none of the measurements on the deformed samples produced the pop-ins that appeared in some of the measurements on the undeformed sample (see Fig. 2d). As discussed earlier, the fact that the pop-ins did not appear in any of the deformed samples indicates that the origin of the pop-ins observed in the pres-

Table 1
Summary of the results for the indentation measurements performed on the 30% and 80% deformed samples. The estimated Y_{ind} in the annealed condition for these grains was calculated from the contoured plot presented in Fig. 3b. The difference between the measured and the estimated indentation yield strengths provides a reliable estimate of the percentage increment in the critical resolved shear strength (τ_{CRSS}) of the slip system.

Region #	Orientation (φ_1, Φ, φ_2)	Misorientation	E_{eff} (GPa)	β	Estimated Y_{ind} in the annealed condition (GPa)	Measured Y_{ind} in the deformed condition (GPa)	% change in τ_{CRSS}
30% Deformed Fe–3%Si							
1	148.3, 49.8, 50.7	7° from (1 1 1)	198.0 ± 3.9	1.09	1.12	1.31 ± 0.13	16.9
2	294.2, 13.5, 83.8	14° from (0 0 1)	174.2 ± 1.59	0.93	0.90	1.07 ± 0.05	18.9
80% Deformed Fe–3%Si							
1	111.6, 49.4, 54.2	20° from (1 1 1)	198.1 ± 1.26	1.09	1.12	1.69 ± 0.06	50.9
2	326.3, 23.2, 58	30° from (0 0 1)	191.1 ± 1.42	1.04	1.00	1.46 ± 0.07	46.0
4	263, 16.2, 73.7	25° from (0 0 1)	185.9 ± 0.75	1.00	0.92	1.37 ± 0.07	48.9
3	259, 3.9, 84.4	10° from (0 0 1)	174.3 ± 0.19	0.93	0.85	1.27 ± 0.08	49.4

ent study can be attributed to scarcity of dislocations in the as-cast sample. This observation has been discussed in detail in our recent report [9].

The indentation measurements on the deformed samples are summarized in Table 1. For each of the grains studied in the deformed sample, we estimated the indentation yield point in the fully annealed condition using the grain orientation and the contoured plot presented in Fig. 3c. In other words, this would have been the indentation yield point if the same grain was in the as-cast sample. As discussed earlier, it is important to establish this value because it can vary by as much as 30% from the near-(0 0 1) "soft" orientations to the near-(1 1 1) "hard" orientations. The difference between the measured indentation yield point and the estimated indentation point in the as-cast condition then provides a reliable estimate of the increment in the indentation yield point at the indentation site. This increment can be attributed to the changes in the dislocation content at the indentation site from its initial state in the as-cast sample.

The simplest relationship one can establish between the increment in the indentation yield point and the local dislocation content is through the increment in the critical resolved shear strength of the slip system. In a highly simplified approach, one could express this relationship as

$$Y_{ind} = M(\Phi, \varphi_2)\, \tau_{CRSS}, \quad \Delta\tau_{CRSS} \propto \sqrt{\rho} \tag{4}$$

where $1/M$ is a Schmid-like factor that depends only on the grain orientation (in the present case only on two of the three Bunge–Euler angles describing the crystal orientation), τ_{CRSS} is the averaged critical resolved shear stress in the crystal, $\Delta\tau_{CRSS}$ is the increment in the local averaged critical resolved shear strength between the as-cast and cold-worked conditions, and ρ is the local dislocation density. Since the factor M is the only orientation dependent variable, it is easy to see that percentage increase in the indentation yield point can be assumed to be equal to the percentage increase in τ_{CRSS}. These are reported in Table 1 for all the measurements in the deformed sample obtained in this study. The percentage increases in τ_{CRSS} provide an indirect measure of the local dislocation content or the local stored energy in the deformed sample. It is seen from the limited number of measurements obtained in this study that the changes in τ_{CRSS} vary significantly from one deformation step to another and also from one region to another in the same deformed sample, resulting in a highly heterogeneous microstructure in the deformed polycrystalline samples. It is also clear from Table 1 that any conclusions drawn regarding the local slip resistance or the local dislocation content directly from the measured indentation yield points without accounting for the effect of the crystal lattice orientation at the indentation site would be highly erroneous in the examples shown here.

5. Conclusions

In summary, we have demonstrated a novel approach to extract meaningful correlations between local crystal lattice orientation measurements obtained from OIM and the estimates of local elastic and yield properties from nanoindentation measurements. This has been made possible by the use of our newly developed data analysis procedures for the conversion of load–displacement data obtained in spherical nanoindentation of polycrystalline cubic metals into indentation stress–strain curves that includes our new procedure for establishing the effective zero-load and zero-displacement point in the raw dataset. In this work, conducted on polycrystalline Fe–3% Si samples but easily extendable to other material systems, our analysis procedures are able to account for the effect of crystal lattice orientation on the indentation modulus and the indentation yield strength of the as-cast samples. Using this information, we are then able to correlate the increment in indentation yield strength to the changes in the slip resistance at the indentation site of the 30% and 80% plastically deformed samples.

Acknowledgements

This work was supported by the National Science Foundation through grant number DMR-0303395. The authors wish to acknowledge many helpful discussions with Prof. Roger Doherty (Drexel University) during the preparation of this manuscript. The MTS XP® System and the TSL-

OIM System (integrated with the ESEM Philips XL 30) used in this study are maintained and operated by the Centralized Research Facilities in the College of Engineering at Drexel University. S.P. also wishes to acknowledge the support from the Sigma Xi Grants-in-Aid of Research (GIAR) program for this work.

References

[1] Fischer-Cripps AC. Nanoindentation. Berlin: Springer; 2004.
[2] Johnson KL. Contact mechanics. Cambridge: Cambridge University Press; 1987.
[3] Tabor D. The hardness of metals. Oxford: Oxford University Press; 1951.
[4] Oliver WC, Pharr GM. J Mater Res 1992;7:1564.
[5] Schuh CA. Mater Today 2006;9:32.
[6] Kalidindi SR, Pathak S. Acta Mater 2008;56:3523.
[7] Pathak S, Kalidindi SR, Klemenz C, Orlovskaya N. J Eur Ceram Soc 2008;28:2213.
[8] Pathak S, Shaffer J, Kalidindi SR. Scripta Mater 2009;60:439.
[9] Pathak S, Stojakovic D, Doherty R, Kalidindi SR. J Mater Res 2009;24(March):1127 [Focus Issue on Nanoindentation].
[10] Bhattacharyya A, El-Danaf E, Kalidindi SR, Doherty RD. Key Eng Mater 2000;177–180:183.
[11] Bhattacharyya A, El-Danaf E, Kalidindi SR, Doherty RD. Int J Plasticity 2001;17:861.
[12] Kalidindi SR, Bhattacharyya A, Doherty RD. Adv Mater 2003;15:1345.
[13] Kalidindi SR, Bhattacharyya A, Doherty RD. Proc Royal Soc London, Ser A: Math, Phys and Eng Sci 2004;460:1935.
[14] Hertz H. Miscellaneous papers. New York: Macmillan & Co. Ltd.; 1896.
[15] Vlassak JJ, Nix WD. Philos Mag A: Phys Condens Matter Defect Mech Propert 1993;67:1045.
[16] Vlassak JJ, Nix WD. J Mech Phys Solids 1994;42:1223.
[17] Proust G, Kalidindi SR. TMS Lett: The Min Met Mater Soc 2004;7:151.
[18] Biener MM, Biener J, Hodge AM, Hamza AV. Phys Rev B: Condens Matter Mater Phys 2007;76:165422.
[19] Pathak S, Go knur Cambaz Z, Kalidindi SR, Gregory Swadener J, Gogotsi Y. Carbon 2009, doi:10.1016/j.carbon.2009.03.042.
[20] Sneddon IN. Int J Eng Sci 1965;3:47.
[21] Farthing LJ, Weihs TP, Kisker DW, Krajewski JJ, Tang MF, Stevenson DA. In: Thin films: stresses and mechanical properties symposium. Boston, MA: Materials Research Society; 1988 [p.123].
[22] Cammarata RC, Schlesinger TE, Kim C, Qadri SB, Edelstein AS. Appl Phys Lett 1990;56:1862.
[23] Vlassak JJ, Ciavarella M, Barber JR, Wang X. J Mech Phys Solids 2003;51:1701.
[24] Willis JR. J Mech Phys Solids 1966;14:163.
[25] Mencik J, Swain MV. J Mater Res 1995;10:1491.
[26] Fischer-Cripps AC. Surf Coat Tech 2006;200:4153.
[27] Chudoba T, Griepentrog M, Duck A, Schneider D, Richter F. J Mate Res 2004;19:301.
[28] Chudoba T, Schwarzer N, Richter F. Surf Coat Tech 2000;127:9.
[29] Linss V, Schwarzer N, Chudoba T, Karniychuk M, Richter F. Surf Coat Tech 2004;195:287.
[30] Richter F, Herrmann M, Molnar F, Chudoba T, Schwarzer N, Keunecke M, et al. Surf Coat Tech 2006;201:3577.
[31] Grau P, Berg G, Fraenzel W, Meinhard H. Phys Status Solidi (A) Appl Res 1994;146:537.
[32] Ullner C. Measurement 2000;27:43.
[33] Oliver WC, Pharr GM. J Mater Res 2004;19:3.
[34] Deuschle J, Enders S, Arzt E. J Mater Res 2007;22:3107.
[35] Basu S, Moseson A, Barsoum MW. J Mater Res 2006;21:2628.
[36] Field JS, Swain MV. J Mater Res 1993;8:297.
[37] Field JS, Swain MV. J Mater Res 1995;10:101.
[38] Murugaiah A, Barsoum MW, Kalidindi SR, Zhen T. J Mater Res 2004;19:1139.
[39] Swain MV. Mater Sci & Eng A: Struct Mate: Propert, Microstruct Process 1998;253:160.
[40] Hashin Z, Shtrikman S. J Mech Phys Solids 1962;10:343.
[41] Bunge H. Texture analysis in materials science. London: Butterworth; 1982.